Research Report

Performance Characteristics of a Thermo-electric Topography Sensor

Abu Sebastian, Dorothea Wiesmann, Christoph Hagleitner and Evangelos Eleftheriou

IBM Research GmbH
Zurich Research Laboratory
8803 Rüschlikon
Switzerland

Performance Characteristics of a Thermo-electric Topography Sensor

Abu Sebastian, Dorothea Wiesmann, Christoph Hagleitner and Evangelos Eleftheriou
IBM Zürich Research Laboratory, CH-8803 Rüschlikon, Switzerland

Abstract— **Micro-fabricated silicon cantilevers with integrated heating elements could be used for topography sensing. In this research report we present the sensitivity, bandwidth and resolution of one of these sensors.**

I. THERMO-ELECTRIC TOPOGRAPHY SENSORS

Thermo-electric topography sensors have been used as read transducers in the probe-based data storage effort pursued by IBM [1], [2], [3], [4]. They could also serve as general purpose topography sensors. The low cost and the ease of integration make them particularly attractive. The schematic of one such micro-fabricated silicon cantilever is shown in figure 1. Resistive heaters are integrated on the cantilever with an effective area of $4\mu \times 4\mu$m. The heaters are produced by varying the doping levels. In the heater region the doping concentration is in the order of $10^{16} - 10^{18}$ cm^{-3}. The legs adjacent to the heaters are highly doped at approximately 10^{20} cm^{-3}. These heaters could be heated by applying an electrical current through the cantilever legs and the heater. Constant voltage excitation is typically employed.
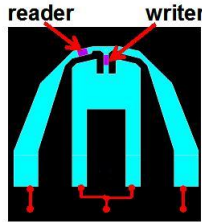

Fig. 1. The schematic of a micro-fabricated silicon cantilever with integrated read and write heating elements.

The heat transportation is primarily through the air-gap between the heater and the sample and through the cantilever legs. The thermo-electric sensing is based on the following two premises. (1) The heat conduction through air depends on the distance of the sensor from the substrate. (2) the resistance of the heater is a strong function of the temperature. As the cantilever tip follows the topographical variations (indentations in the case of probe storage devices), the distance of the read heater from the substrate gets modulated by the topographical variations. This translates to a difference in cooling which indeed results in a change of the electrical resistance of the heater. In the case of constant voltage excitation, the change in resistance can be measured as a change in the current.

II. MODELING AND IDENTIFICATION

To experimentally identify the sensitivity, bandwidth and resolution, we primarily rely on an operator model of the sensors [5].

The two key assumptions that are made in the operator model are,
1) The operator relating the temperature with the input power is linear.
2) The operator relating the electrical resistance to temperature is memoryless but could be nonlinear.
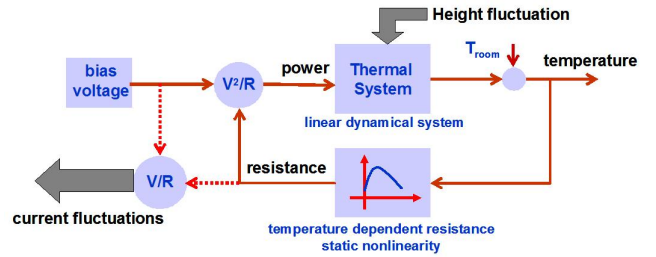

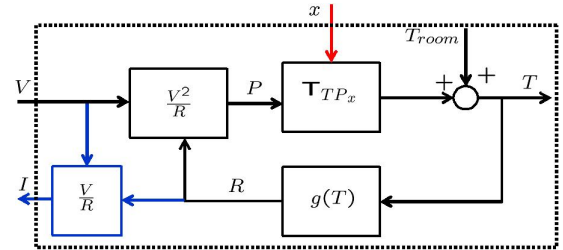Fig. 2. A descriptive model for the micro-heaters.

Fig. 3. The model for the micro-heaters.

A descriptive model of the micro-heater is presented in Figure 2. The corresponding block diagram representation is shown in Figure 3. The main components are a linear operator relating power with temperature and a nonlinear operator relating the temperature with electrical resistance. The linear operator relating the input power to the temperature is denoted by $\mathbf{T}_{TP_x}$. $\mathbf{T}_{TP_x}$ captures the dynamics of thermal conduction as a function of the power dissipated in the heating elements when the heater sample separation equals x. Specifically $\mathbf{T}_{TP_x}$ captures the thermal system for that particular x. The function $g(.)$ models the memoryless nonlinear relationship between temperature and the electrical resistance. This function $g(.)$ is typically a bell shaped curve with the resistance value reaching a maximum at a certain temperature T_{max}. Below T_{max}, the resistance increases with temperature because of a corresponding decrease of mobility of the majority carriers. However, above T_{max}, the resistance becomes smaller with

increasing temperature owing to the predominance of the thermally activated increase of carrier density.

The signal that could be measured experimentally is the current which is the input voltage divided by the resistance of the heater. Note that it is assumed that the resistance of the cantilever is dominated by the resistance of the heating elements and that the input power is almost completely dissipated in the heaters.
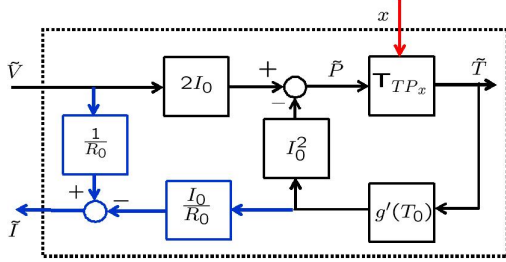

Fig. 4. The linearized model for the micro-heaters.

For small signal analysis one could linearize the various nonlinear blocks and obtain a linear model as shown in Figure 4. Such a linear model facilitates the calculation of transfer functions relating the signals of interest. R_0, I_0 and T_0 are the resistance, current and temperature values at the operating point. $g'(T_0)$ denotes the slope of $g(.)$ at T_0.
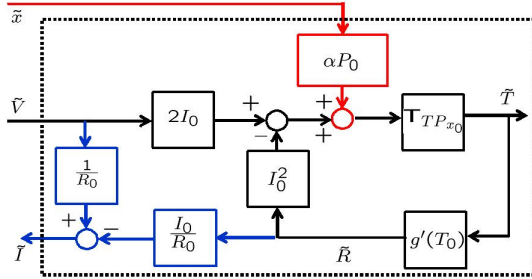

Fig. 5. The model for the micro-heater where the perturbation of $\mathbf{T}_{TP_x}$ is cast as an input to the feedback system. $\alpha = \frac{K'(x)}{K(x)}$.

For topography sensing the operator of interest is $\mathbf{T}_{\tilde{I}\tilde{x}_x}$, which relates the fluctuation of the current to the fluctuation of the heater-sample separation about an operating point of heater-sample separation, x_0. The heater-sample separation, $\tilde{x}$ modifies the operator $\mathbf{T}_{TP_x}$. This perturbation of the thermal system is detected by monitoring the current fluctuations. Thermo-mechanical sensing can be viewed in the context of the general class of problems where the perturbation of a linear time invariant system is detected by monitoring signals within a feedback configuration it is part of. The efficiency (sensitivity) and speed (bandwidth) of detection of this change could be studied using linear transfer functions.

Assuming that the gain perturbation of the operator $\mathbf{T}_{TP_x}$ due to $\tilde{x}$ is primarily responsible for topography sensing $\tilde{x}$ enters the feedback loop as another input. The resulting system is depicted in Figure 5. The sensing transfer function is then

given by

$$\mathbf{T}_{\tilde{I}\tilde{x}_x} = \frac{K'(x)}{K(x)}\left(\frac{-I_0}{R_0}\frac{g'(T_0)P_0\mathbf{T}_{TP_x}}{1+I_0^2 g'(T_0)\mathbf{T}_{TP_x}}\right) \qquad (1)$$

where $K(x)$ is the gain of the thermal system as a function of heater-sample separation. $\mathbf{T}_{\tilde{I}\tilde{x}_x}$ provides the sensitivity and bandwidth of topography sensing.
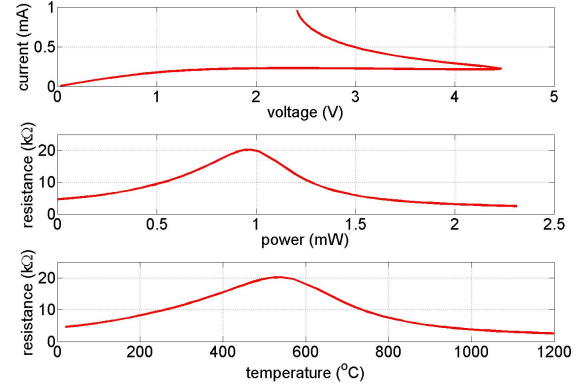

Fig. 6. Typical voltage Vs. current, power Vs. resistance and temperature Vs. resistance curves are shown.

The first step in the identification process is the identification of $g(.)$, the operator that captures the relationship between the temperature variation and the resistance variation. $g(.)$ is assumed to memoryless (first assumption) and hence could be identified in a quasi-static manner. This is particularly advantageous since it is always possible to measure the variation of current with voltage sufficiently slow so that the thermal dynamics could be ignored. In a typical experiment, a ramp voltage signal is applied to the heater and the corresponding current is measured. From the voltage and current signals it is straight forward to obtain the power Vs. resistance map. From the second assumption, there is a linear relationship between the power and the temperature. Moreover, the temperature corresponding to the maximum resistance is known from the doping levels. Using these two facts, the temperature Vs. resistance map could be obtained (see Figure 6). A polynomial relation, $g(.)$ could be used to capture the temperature Vs. resistance relationship.

The next step in the identification process is that of the linear operator $\mathbf{T}_{TP_x}$. From the linearity, the frequency response completely characterizes the operator. Moreover, the identification is independent of the operating voltage. There are two ways to identify $\mathbf{T}_{TP_x}$. A DC voltage with a small amplitude noise or chirp signal added on top is applied to the heater. The corresponding current fluctuation is measured. The resistance fluctuation could be obtained from the voltage and current measurements. Using the identified relationship between temperature and resistance, $g(.)$, the temperature fluctuation could be obtained as $\tilde{T} = g^{-1}(R) - g^{-1}(R_0)$. The power fluctuation is measured as $\tilde{P} = VI - V_0I_0$. From $\tilde{P}$ and $\tilde{T}$, the frequency response of $\mathbf{T}_{TP_x}$ could be obtained as,

$$\mathbf{T}_{TP_x}(j\omega) = \frac{C_{\tilde{P}\tilde{T}}(j\omega)}{C_{\tilde{P}\tilde{P}}(j\omega)} \qquad (2)$$

where $C_{\tilde{P}\tilde{T}}(j\omega)$ denotes the cross-covariance between $\tilde{P}(t)$ and $\tilde{T}(t)$ and $C_{\tilde{P}\tilde{P}}(j\omega)$ denotes the auto-covariance of the stochastic process $\tilde{P}(t)$. A stable proper transfer function could be used to fit the experimentally measured frequency response.
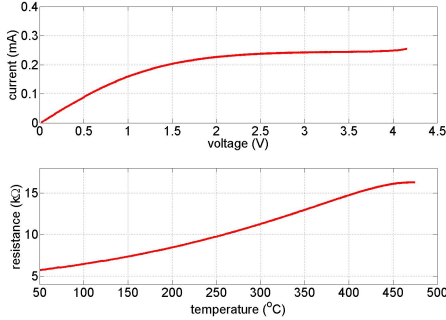
III. SENSITIVITY AND BANDWIDTH

Fig. 7. The current vs. voltage relationship and the resulting resistance vs. temperature map.

The static relationship between voltage and current was first obtained (see Figure 7). From this relationship and the fact that the maximum resistance occurs at a temperature of 472^oC, the nonlinear relationship between the temperature and resistance was obtained. An 8th order polynomial was used to capture this relationship.
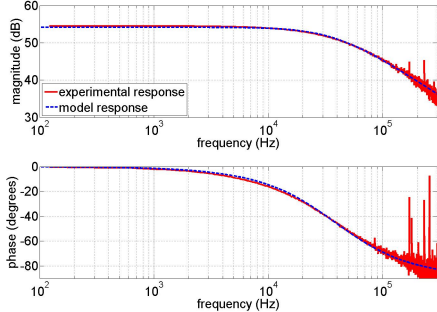

Fig. 8. The experimentally obtained frequency response is compared with that obtained from a model.

A 50mV chirp signal offset by 1V was used for the identification of $\mathbf{T}_{TP_x}$. The micro-cantilever was brought into contact with a polymer sample. This fixed the heater-sample separation to be the height of the tip which is approximately 500 nm. The thermal system was identified using the direct method and a first order transfer function was found to capture the experimental frequency response given by,

$$\mathbf{T}_{TP_x}(s) = \frac{378.7}{3 \times 10^{-6}s + 1}$$

The experimental frequency response is compared with model response in Figure 8. Since a first order model adequately captures the dynamics of $\mathbf{T}_{TP_x}$, one could even talk in terms of time constants.

In order to derive the sensing transfer function we have to identify the variation of the thermal system as a function of
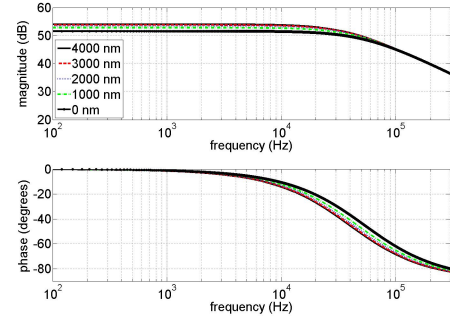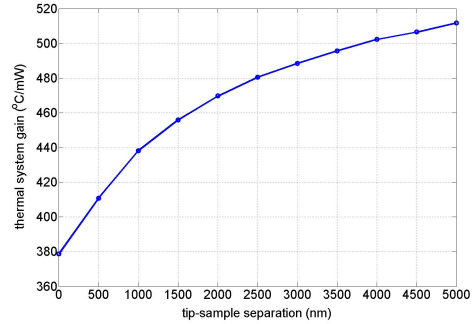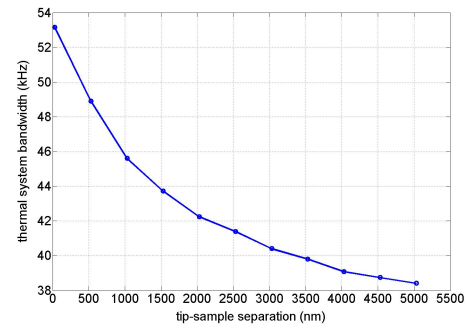

Fig. 9. The variation $\mathbf{T}_{TP_x}$ as a function of the cantilever tip-sample separation.

the heater-sample separation. As described earlier, it is the change in the thermal system that we monitor in the form of a change in the electrical resistance or a subsequent change in the current. As the heater-sample separation is increased, intuitively the linear thermal system should become slower since the conduction path through the air gap between the heater and the substrate is getting longer. Moreover, since the heater is getting more thermally isolated, for a given power input the heater should heat up to a higher temperature. This is precisely what is observed experimentally. Figure 9 shows the variation of $\mathbf{T}_{TP_x}$ as a function of heater-sample separation. The change in the gain and bandwidth is shown in Figure 10. Here the bandwidth is defined to be the -3 dB cut-off frequency.
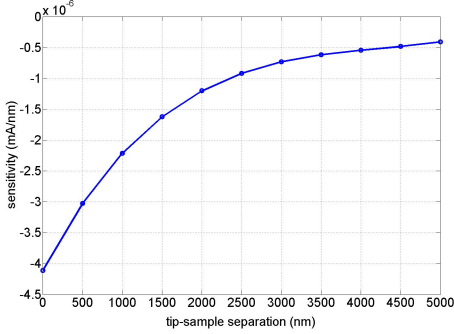

(a)

(b)

Fig. 10. (a) The variation of the gain of $\mathbf{T}_{TP_x}$ as a function of heater-sample separation is shown. (b) The variation of the bandwidth of $\mathbf{T}_{TP_x}$ as a function of heater-sample separation is shown.

In order to obtain the sensing transfer function the relation-

ship given by Equation (1) is used. For the read transducer the transfer function of importance is the sensing transfer function, $\mathbf{T}_{\tilde{I}\tilde{x}_x}$. The relationship given by Equation 1 is used to derive $\mathbf{T}_{\tilde{I}\tilde{x}_x}$. From the gain variation of the thermal system as a function of heater-sample separation (Figure 10(a)) $\alpha = \frac{K'(x)}{K(x)}$ is evaluated. Using (1), $\mathbf{T}_{\tilde{I}\tilde{x}_x}$ is evaluated at various heater-sample separations. In particular $\mathbf{T}_{\tilde{I}\tilde{x}_x}$ while the tip is in contact with the sample is given by,

$$\mathbf{T}_{\tilde{I}\tilde{x}_x}(s) = \frac{-9.844 \times 10^{-6}}{2.281 \times 10^{-6} s + 1}$$

(a)
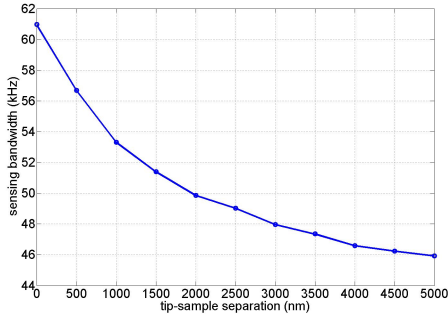
(b)

Fig. 11. (a) The variation of the gain of $\mathbf{T}_{\tilde{I}\tilde{x}_x}$ as a function of heater-sample separation is shown. (b) The variation of the bandwidth of $\mathbf{T}_{\tilde{I}\tilde{x}_x}$ as a function of heater-sample separation is shown.
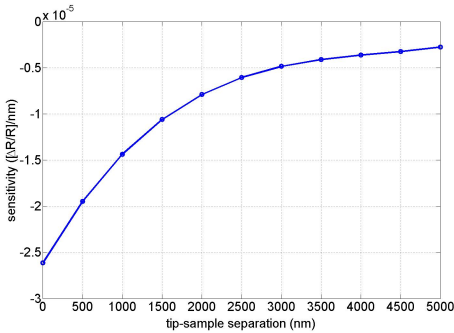

Fig. 12. Sensitivity depicted in terms of $\Delta R/R$.

The sensing transfer functions were evaluated at other tip-sample separations (subsequent heater-sample separations) and the results are shown in Figure 11. It can be seen that the sensitivity and bandwidth both deteriorate as the heater-sample

separation increases. Sensitivity can also be specified in terms of $\Delta R/R$. This is shown in Figure 12.
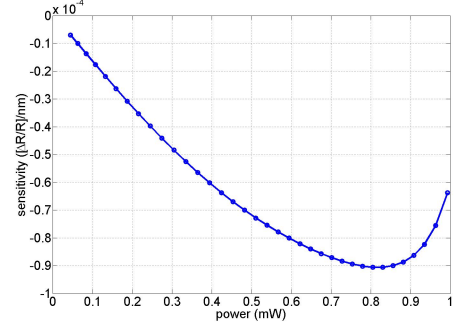
(a)
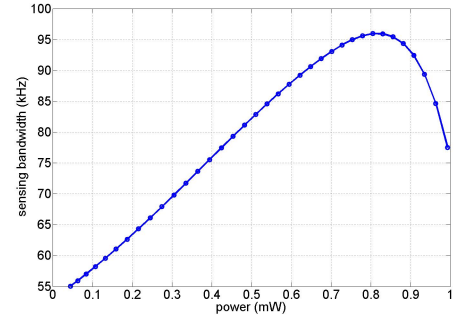
(b)

Fig. 13. (a) The variation of sensitivity as a function of power. (b) The variation of sensing bandwidth as a function of power.

The relation (1) also provides a straight forward means of ascertaining the sensitivity and bandwidth variations as a function of bias voltage or power. The sensitivity and bandwidth variation as a function of the power is presented in 13(a) and (b).

IV. RESOLUTION

The dominant noise sources in thermo-electric sensing are the thermal noise of the silicon resistor and $1/f$-noise. The $1/f$ noise contribution is more difficult to predict. This conductance fluctuation noise is typically described by a model developed by Hooge that relates the $1/f$ noise to the number of carriers in the bulk of the resistor and assumes that it is proportional to the dissipated power. Let n_{R_j} represent the thermal noise and let n_{R_f} denote the $1/f$ noise component. Both random processes are thought of as equivalent resistance fluctuations. Let $S_{n_{R_j}}$ be the power spectral function corresponding to n_{R_j} given by,

$$S_{n_{R_j}}(f) = \frac{4k_B T_0 R_0^2}{P_0} \quad (3)$$

where k_B is the Boltzmann constant. Let $S_{n_{R_f}}$ denote the power spectral function corresponding to rn_f given by,

$$S_{n_{R_f}}(f) = \frac{\alpha}{f N_{carr}} \quad (4)$$

where α denotes the Hooge factor and N_{carr} denotes the number of carriers in the bulk of the resistor. The net resistance
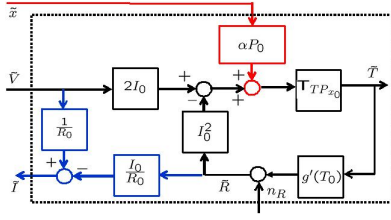
Fig. 14. Block diagram depicting the influence of resistance noise

noise is the sum of these two noise sources given by $n_R = n_{R_j} + n_{R_f}$.

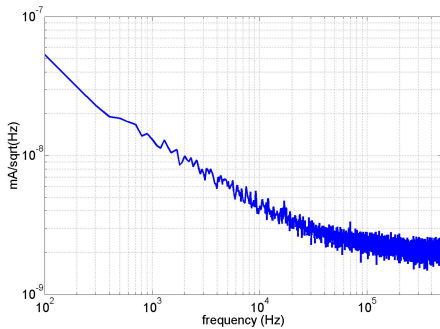The resistance noise enters the system as shown in Figure 14. The resulting current fluctuation is given by,

$$\tilde{I} = \frac{-I_0/R_0}{1 + I_0^2 g'(T_0)\mathbf{T}_{TP_x}} n_R$$
$$= \mathbf{T}_{\tilde{I}n_{R_x}} n_R$$

Note that owing to the electrical feedback, the measured resistance fluctuation is slightly different from the "input" resistance fluctuation given by,

$$\tilde{R} = \frac{1}{1 + I_0^2 g'(T_0)\mathbf{T}_{TP_x}} n_R \qquad (5)$$
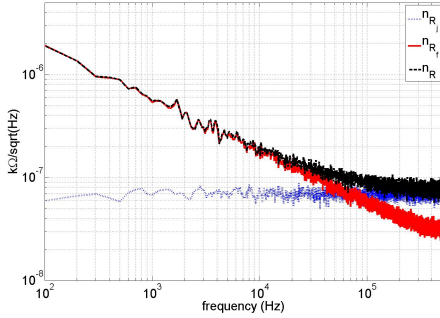
(a)

(b)

Fig. 15. (a) Simulated Johnson noise and $1/f$ noise and the resulting input resistance fluctuation (b) The simulated current fluctuation resulting from the input resistance fluctuation

For a Hooge factor $\alpha = 1 \times 10^{-5}$, carrier density of $2 \times 10^{17}/cm^3$ and heater dimensions of $2\mu m \times 6\mu m \times 0.5\mu m$, the power spectra of the input resistance fluctuation is depicted in Figure 15(a). The resulting simulated current fluctuation is depicted in Figure 15(b).
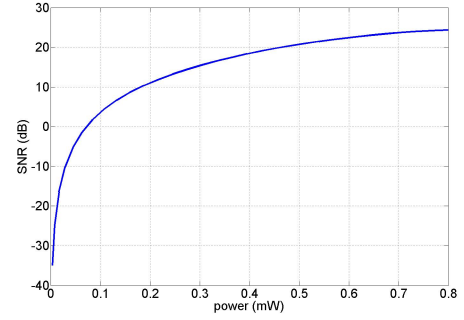

Fig. 16. The projected SNR variation as a function of the power.

The signal to noise ratio per nanometer is given by,

$$SNR = 20log \left(\frac{\sqrt{\int_{BW} |\mathbf{T}_{\tilde{I}\tilde{x}_x}(f)|^2 df}}{\sqrt{\int_{BW} |\mathbf{T}_{\tilde{I}n_{R_x}}(f)|^2 S_{n_R}(f) df}} \right) \qquad (6)$$

For the simulations presented here, the SNR is obtained to be 7.8 dB/nm for a power of 0.159 mW and for a bandwidth, BW = 100kHz. As in the case of sensitivity and bandwidth, the relation (1) can be used to obtain the SNR variation as a function of the applied voltage or power. The variation of SNR as a function of power is depicted in Figure 16.
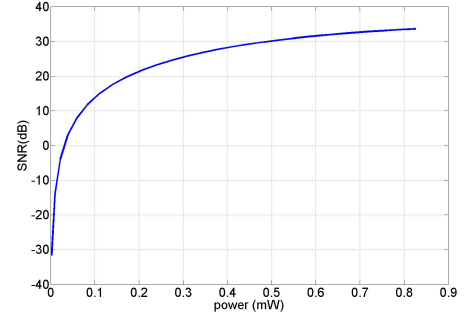

Fig. 17. Lumped parameter simulation results on SNR as a function of power
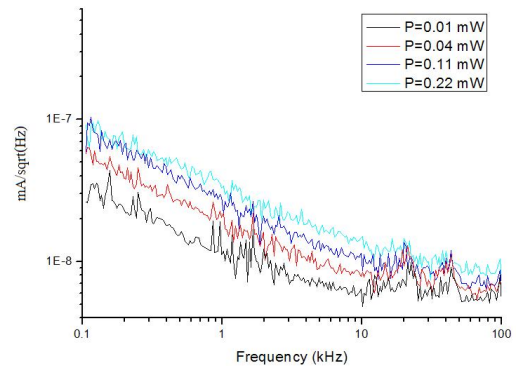

Fig. 18. Experimentally measured noise induced current fluctuations

A lumped element model of the sensor implemented in Verilog-A is presented in [6]. Simulation results of this partic-

ular topography sensor obtained using this model are presented in Figure 17. It can be seen that these results compare favorably with those presented in Figure 16. Experimentally measured current fluctuations at different power levels are shown in Figure 18. The slightly higher noise levels indicate the presence of other noise sources besides the ones used in our simulations.

V. OUTLOOK FOR THE FUTURE

We have assessed the potential to further increase SNR and thus resolution at high bandwidth with numerical simulations [6]. The main design variations leading to higher sensing bandwidths are the decrease of heated volume, i.e. width, length, and thickness of the heater, and the increase of heat conduction towards the substrate, i.e. improvement of boundary layer resistance and decrease of distance between heater and substrate.

The main drawback when decreasing the volume of the heater is the increase of $1/f$-noise. However, it has been observed that the Hooge factor is highly fabrication process dependent. In silicon cantilevers, values as low as 3×10^{-6} have been measured. We have been able to achieve Hooge factors as low as 8×10^{-6}. For our simulations we have assumed two scenarios: a moderate improvement of Hooge factor to 1×10^{-5} and an aggressive target of 1×10^{-6}.
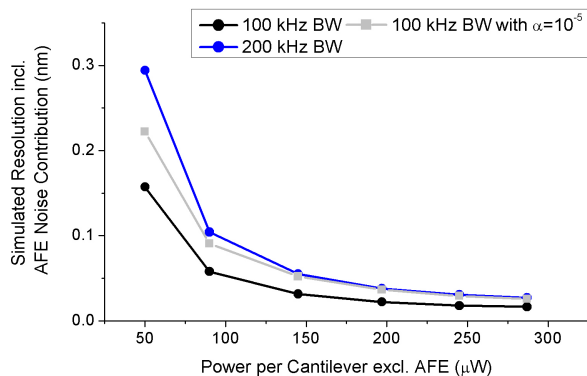

Fig. 19. Simulated resolution for different bandwidths and Hooge factors.

Figure 19 shows the simulated resolution as a function of power applied to the cantilever (heating power) for a BW of 100 kHz and 200 kHz, black and blue line, respectively for an assumed Hooge factor of 1×10^{-6}. The grey line denotes the resolution for a BW of 100 kHz for an assumed Hooge factor of 1×10^{-5}. It can be seen that sub-Angstrom resolution is possible with a BW of 200 kHz even without achieving the aggressive Hooge factor target.

REFERENCES

[1] P. Vettiger, G. Cross, M. Despont, U. Drechsler, U. Dürig, B. Gotsmann, W. Häberle, M. Lantz, H. Rothuizen, R. Stutz, and G. Binnig, "The "millipede"-nanotechnology entering data storage," *IEEE Transactions on Nanotechnology*, vol. 1, pp. 39–55, 2002.

[2] E. Eleftheriou, T. Antonakopoulos, G. K. Binnig, G. Cherubini, M. Despont, A. Dholakia, U. Dürig, M. A. Lantz, H. Pozidis, H. E. Rothuizen, and P. Vettiger, "Millipede-a MEMS based scanning-probe data storage system," *IEEE Transactions on Magnetics*, vol. 39(2), pp. 938–945, 2003.

[3] M. Despont, U. Drechsler, R. R. Yu, B. H. Pogge, and P. Vettiger, "Wafer-scale microdevice transfer/interconnect: From a new integration method to its application in an AFM-based data-storage system," *Journal of Microelectromechanical Systems*, vol. 13(6), pp. 895–901, 2004.

[4] U. Dürig, "Fundamentals of micro-mechanical thermo-electric sensors," *Journal of Applied Physics*, vol. 98, p. 044906, 2005.

[5] D. Wiesmann and A. Sebastian, "Dynamics of silicon micro-heaters: Modeling and experimental identification," in *Proceedings of the IEEE MEMS Conference*, February 2006, pp. 182–185.

[6] C. Hagleitner, T. Bonaccio, H. Rothuizen, J. Lienemann, D. Wiesmann, G. Cherubini, J. G. Korvink, and E. Eleftheriou, "Modeling, design and verification for the analog front-end of a mems-based parallel scanning-probe storage device," *to appear IEEE Journal of Solid State Circuits*, vol. 42(8), 2007.